

PAPER • OPEN ACCESS

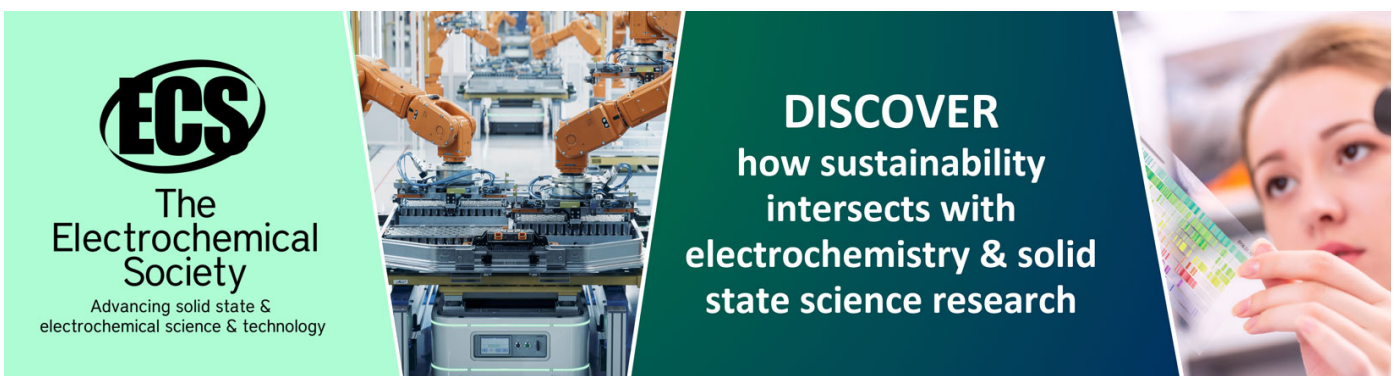
Hydrogen diffusion and local Volta potential in high- and medium-entropy alloys

To cite this article: M Rhode *et al* 2020 *IOP Conf. Ser.: Mater. Sci. Eng.* **882** 012015

View the [article online](#) for updates and enhancements.

You may also like

- [Plastic deformation and strengthening mechanism of FCC/HCP nano-laminated dual-phase CoCrFeMnNi high entropy alloy](#)
Cheng Huang, Yin Yao, Xianghe Peng et al.
- [Structural and thermal properties of nanocrystalline Al_{1-x}\(SiFeCoNi\)_{100-x} medium entropy alloys](#)
Amina Hana, Naveed Kausar Janjua, Tayyab Subhani et al.
- [Review—Corrosion-Resistant High-Entropy Alloy Coatings: A Review](#)
Hongxu Cheng, Zhimin Pan, Yu Fu et al.



ECS
The
Electrochemical
Society
Advancing solid state &
electrochemical science & technology

DISCOVER
how sustainability
intersects with
electrochemistry & solid
state science research

Corrigendum

Corrigendum: Hydrogen diffusion and local Volta potential in high- and medium-entropy alloys

(2020 IOP Conf. Ser.: Mater. Sci. Eng. **882** 012015)

M Rhode^{1,3}, A Wetzel², O Ozcan², J Nietzke^{1,3}, T Richter¹, D Schroeppfer¹

¹ Department 9 - Component Safety, Bundesanstalt für Materialforschung und -prüfung (BAM), Unter den Eichen 87, 12205 Berlin, Germany

² Department 6 - Materials Chemistry, Bundesanstalt für Materialforschung und -prüfung (BAM), Unter den Eichen 87, 12205 Berlin, Germany

³ Institute for Materials Science and Joining Technology, Otto-von-Guericke University, Universitätsplatz 2, 39106 Magdeburg, Germany

Page 3:

In the sub-section “2.1 Investigated materials” the following content appears:

Table 1. Chemical composition (in atomic %) of the CoCrFeMnNi-HEA and CoCrNi-MEA.

Alloy	Co	Cr	Fe	Mn	Ni
HEA	20.7	20.1	19.6	19.7	19.9
MEA	34.3	-	-	33.0	32.7

The chemical composition of Co, Cr and Mn was in wrong order in this previous version for both HEA and MEA. The table 1 content in corrected form should read:

Table 1. Chemical composition (in atomic %) of the CoCrFeMnNi-HEA and CoCrNi-MEA.

Alloy	Co	Cr	Fe	Mn	Ni
HEA	19.7	20.7	19.6	20.1	19.9
MEA	33.0	34.3	-	-	32.7



Hydrogen diffusion and local Volta potential in high- and medium-entropy alloys

M Rhode^{1,3}, A Wetzel², O Ozcan², J Nietzsche^{1,3}, T Richter¹ and D Schroepfer¹

¹ Department 9 - Component Safety, Bundesanstalt für Materialforschung und -prüfung (BAM), Unter den Eichen 87, 12205 Berlin, Germany

² Department 6 - Materials Chemistry, Bundesanstalt für Materialforschung und -prüfung (BAM), Unter den Eichen 87, 12205 Berlin, Germany

³ Institute for Materials and Joining Technology, Faculty of Mechanical Engineering Otto-von-Guericke University, Universitätsplatz 2, 39106 Magdeburg, Germany

michael.rhode@bam.de / michael.rhode@ovgu.de

Abstract. High-entropy alloys (HEAs) are characterized by a solid solution of minimum five and medium-entropy alloys (MEAs) of minimum three principal alloying elements in equiatomic proportions. They show exceptional application properties, such as high-strength and ductility or corrosion resistance. Future HEA/MEA-components could be exposed to hydrogen containing environments like vessels for cryogenic or high-pressure storage where the hydrogen absorption and diffusion in these materials is of interest. In our study, we investigated the HEA $\text{Co}_{20}\text{Cr}_{20}\text{Fe}_{20}\text{Mn}_{20}\text{Ni}_{20}$ and the MEA $\text{Co}_{33.3}\text{Cr}_{33.3}\text{Ni}_{33.3}$. For hydrogen ingress, cathodic charging was applied and diffusion kinetic was measured by high-resolution thermal desorption spectroscopy using different heating rates up to 0.250 K/s. Peak deconvolution resulted in high-temperature desorption peaks and hydrogen trapping above 280 °C. A total hydrogen concentration > 40 ppm was identified for the MEA and > 100 ppm for HEA. This indicates two important effects: (1) delayed hydrogen diffusion and (2) considerable amount of trapped hydrogen that must be anticipated for hydrogen assisted cracking phenomenon. Local electrochemical Volta potential maps had been measured for the hydrogen free condition by means of high-resolution Scanning Kelvin Probe Force Microscopy (SKPFM).

1 Introduction

1.1 High-entropy alloys (HEAs)

High-entropy alloys (HEA) represent a new class of materials consisting of single-phase and disordered solid solutions of alloying elements (in accordance to the taxonomy initially suggested in [1]). They usually have a chemical composition of minimum five alloying elements, whereas so-called medium-entropy alloys (MEAs) comprise two to four alloying elements. In a narrow meaning, HEA or MEA encompasses equiatomic amounts of the specific alloying elements a solid solution in a single-phase microstructure (like fcc) without further precipitates or inclusions. These materials are fundamentally different from conventional alloys that are based on one principal element such as Fe in case of steels, or Al- or Ni-based superalloys. The face-centered cubic (fcc) CoCrFeMnNi material system and its derivatives have been intensively studied and possess excellent mechanical properties, i.e. high ductility, ultimate tensile strength and fracture toughness [2-4]. Among the equiatomic fcc alloys, CrMnFeCoNi-HEA and CrCoNi-MEA are considered as potential structural alloys and get more and



more attention in materials science and engineering [5,6]. For that purpose, HEA and MEA application properties are of great interest.

1.2 Hydrogen absorption and diffusion in HEAs

One of the application properties characteristics of HEAs could be the resistance against hydrogen related degradation of the mechanical properties (some authors also referred to as “hydrogen embrittlement”). The literature study shows the excellent mechanical properties of CoCrFeMnNi-HEA and CoCrNi-MEA alloy in hydrogen containing environments [7-10]. This demonstrates their potential for the use in hydrogen environments as found in vessels for cryogenic or high-pressure storage and is characterized by their outstanding resistance to hydrogen assisted degradation of the mechanical properties. Even at very high hydrogen concentrations (above 30 to 40 ppm) the degradation is low, considering that comparable concentrations are already high enough to remarkably decrease the mechanical properties of other fcc-alloys like Fe-based and high-alloyed austenitic steels [7,9]. For that reason, the hydrogen absorption, diffusion and trapping in these materials is of high interest. Hydrogen can interact with crystal lattice defects (vacancies, dislocations, etc.) and can be bound to so-called traps [11]. This interaction can be expressed by the delayed diffusion compared to not-affected lattice diffusion in pure metals [12]. Generally, a critical combination of a susceptible microstructure, mechanical load and hydrogen concentration is responsible for hydrogen assisted cracking/hydrogen embrittlement [13,14]. First publications on CoCrFeMnNi-HEA showed that hydrogen diffusion at room temperature is comparable to low-carbon version of austenitic stainless steel 316L (X2CrNiMo17-12-2) at 27 °C [15]. Nonetheless, it can be concluded that hydrogen diffusion in HEA and austenitic steel are comparable, the values of the diffusion coefficients have been in the order of 10^{-6} mm²/s, which is contrary to other studies ranging from 10^{-9} to 10^{-8} mm²/s [16,17]. The hydrogen release temperature was also comparable to austenitic stainless steels, which lies between 200 to 450 °C with a maximum peak around 300 °C, whereas the CoCrFeMnNi-HEA trapped significantly more hydrogen (up to 70 ppm). Systematic literature studies on diffusion characteristics and hydrogen release temperatures are rare so far for CoCrFeMnNi-HEA and entirely missing for CoCrNi-MEA. These parameters are important for service conditions of components, namely hydrogen leakage rates by permeating hydrogen at different temperatures.

1.3 Corrosion of HEAs

HEA systems composed of passivating elements, such as Cr, Mo, Ni, Ti, tend to form protective passive oxide layers which show a positive impact on the pitting potential. Even though most HEAs (in case of more than one phase also considered as chemically complex alloys / CCAs) have adequate resistance to general corrosion, microstructural heterogeneities may also result in high susceptibility to localized corrosion [18]. It has been reported that the addition of Al, Cu, Mo and B in HEAs leads to the formation of non-uniform passive films with low corrosion resistance of HEAs [19,20]. Systems including additional Al improve the mechanical properties of CCAs [21], but also lead to the formation of bcc phases and segregation of elements. CoCrFeMnNi-HEA is assumed to be more resistant to pitting corrosion, since it is Al-free and has single-phase fcc-structure [22,23]. Nonetheless, existing literature studies show contradicting results. In [24], the CoCrFeMnNi was compared to 316L steel during immersion tests in NaCl solution with CO₂. A lower corrosion resistance compared to 304 stainless steel in H₂SO₄ was reported [25]. Hence, it is of interest to identify the local corrosion behavior of the HEA and MEA materials depending on their microstructure and chemical composition. In addition, hydrogen can be generated during corrosion in acids as a result of the cathodic part of the corrosion reaction, especially in acidified pits or crevices [26,27] and be introduced into the microstructure and stimulate, or initiate hydrogen assisted stress corrosion cracking (if a sufficiently high mechanical load is applied). Continuous hydrogen charging was applied on CoCrFeMnNi tensile samples but did not result in any remarkable degradation of the mechanical properties [9]. But it must be anticipated that due to the applied strain rate (10^{-4} 1/s) breakdown of the passive layer occurred but test speed was perhaps too high for stress corrosion cracking as hydrogen could not diffuse fast enough.

The presented brief literature review demonstrates that HEA/MEA behavior in the presence of hydrogen is still an open question and demands further investigations. This is particularly the case for MEAs. For that reason, we examined and compared two different equiatomic alloys and their behavior towards absorbed hydrogen, high-temperature diffusion and local electrochemical potentials.

2 Materials and methods

2.1 Investigated materials

In our study, we investigated two different materials, the common five-elements CoCrFeMnNi-HEA (so-called ‘‘Cantor’’-alloy and a three-elements CoCrNi-MEA. We used vacuum melted ingots that have been manufactured by the group of Prof. G. Laplanche (Ruhr-University Bochum). Both alloys had been homogenized after casting and recrystallized for 1 h (CoCrFeMnNi-HEA at 1020 °C and CoCrNi-MEA at 1060 °C) resulting a single-phase fcc-microstructure with an average grain size of 50 μm . More details on alloy preparation and microstructure features can be found elsewhere in [28]. Table 1 shows the chemical composition (in at.-%) of the investigated alloys as determined by electron microprobe analysis (EMPA, with experimental error of about 1 at.-%).

Table 1. Chemical composition (in atomic %) of the CoCrFeMnNi-HEA and CoCrNi-MEA.

Alloy	Co	Cr	Fe	Mn	Ni
HEA	20.7	20.1	19.6	19.7	19.9
MEA	34.3	-	-	33.0	32.7

Specimens with the shape of a circular sector had been used for the experiments. For that purpose, the material rods had been sliced to disks with a thickness of 2 mm and subsequently cut to the final size by electrical discharge machining. The reason was the necessary economic use of the expensive raw materials and high-sophisticated processing of the experimental materials as the sliced disks had been additionally used for milling experiments vs. degradation of surface properties additionally for experiments presented in [29]. The dimensions are described in figure 1 (a).

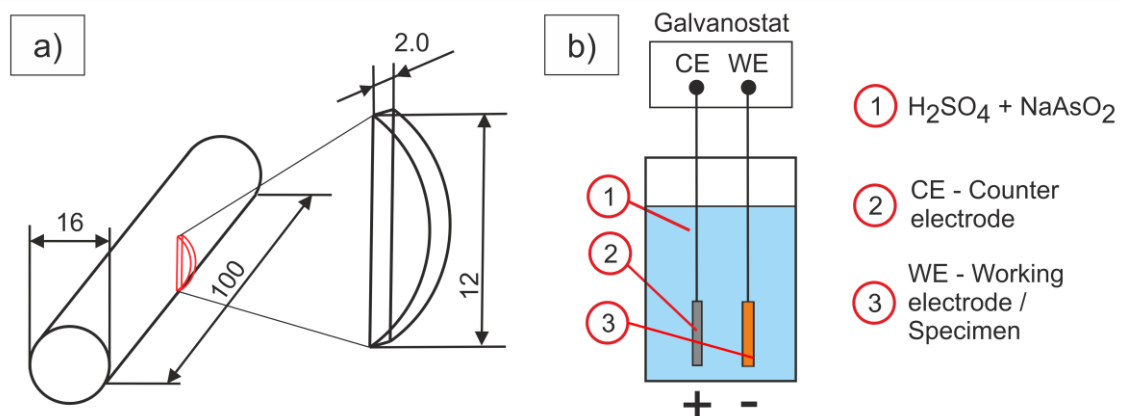


Figure 1. (a) Cut position of flat sample in material rod, dimensions of examined samples and (b) cathodic hydrogen charging set-up.

2.2 Hydrogen charging, measurement and thermal desorption spectroscopy

The samples have been cathodically charged with hydrogen in 0.1 M H₂SO₄ aqueous solution with addition of 0.05 M NaAsO₂ as a recombination inhibitor to increase hydrogen absorption in the materials, see figure 1(b). The sample was the working electrode (WE) and the counter electrode (CE) was a Pt 1800 electrode (SI Analytics), connected to a Wenking Potentiostat/Galvanostat TG94. Before charging,

each specimen surface was manually ground by 500 SiC grit paper, cleaned in ethanol using an ultrasonic bath and rinsed in dry nitrogen gas flow. To ensure an almost homogenous hydrogen distribution, different combinations of charging current density and charging time have been tested. As a result, a galvanostatic charging current of 50 mA/cm² was applied for 240 hours (10 days) to both CoCrFeMnNi and CoCrNi, assuming a low hydrogen diffusivity like in case of austenitic stainless steels. For each material and heating rate two samples have been charged and tested (due to the limited amount of available sample material). The trapping and desorption characteristics were analyzed by BRUKER G8 Galileo using the so-called carrier gas hot extraction technique (CGHE). This analyzer uses an infrared radiation furnace placed around a quartz glass tube. In this tube the sample is placed, heated and the hydrogen desorbs from the sample. The hydrogen is collected in an inert gas (nitrogen) flow and carried to the coupled quadrupole mass spectrometer (MS). The desorbing hydrogen corresponds to a monitored ion current in A (see figure 3 to figure 6). This ion current is integrated within the monitored time range and corresponds to the absolute hydrogen amount that was absorbed by the sample. Via a previously determined calibration factor and the sample weight, the corresponding hydrogen concentration can be calculated in ppm. Further details on CGHE can be found in [30-33]. The temperature was measured using samples with same dimensions and attached type-K thermocouple at the surface. These investigations ensured that the surface temperature corresponds to the programmed heating rate. Deviation of the adjusted and measured temperature is less than 2 K (and therefore ignored in the data analysis). For that reason, the quasi-linear temperature profiles could be idealized and are used for the correlation of the peak temperatures and the corresponding temperature at the sample surface (see figure 3 to figure 6).

Thermal desorption spectroscopy (TDS) can be used to determine effects of microstructure and temperature on hydrogen trapping. In our study, we determined the corresponding desorption spectra using heating rates of $\Phi = 0.125$ and 0.250 K/s. The starting temperature was 25 °C and the final temperature was 450 °C. Subsequently, the samples were hold at 450 °C for at least 10 minutes to potentially desorb very deeply trapped hydrogen (which was not the case). These temperature dependent desorption spectra are the sum of overlapped single peaks with assumed Gaussian distribution. These had been identified and analyzed individually by a peak deconvolution technique using the Gaussian peak fit function of the software Origin 9.7. The result is that each peak can be correlated to a specific peak temperature T_p (maximum effusion), which indicates an activation energy for hydrogen diffusion, i.e. release of trapped hydrogen. In general, the desorption peak shifts to higher temperatures with increasing Φ . Ideally, each Gaussian peak represents a type of a major trap-site in the material (2D or 3D-lattice defects).

2.3 Scanning Kelvin Force Probe Microscopy (SKPFM) analysis

Atomic Force Microscopy (AFM) based Scanning Kelvin Force Probe Microscopy (SKPFM) allows the analysis of Volta-Potential differences on heterogeneous alloy surfaces and at buried metal-polymer interfaces [34,35]. In the Kelvin mode, the surface potential of the sample is measured in addition to the sample topography. Alternating line scans in topography and SKPFM lift mode are carried out, where the tip follows the measured height profile with a constant distance to the surface at a constant DC bias and a superimposed AC bias. The AC bias generates an alternating charging between SKPFM tip and sample surface, which induces an alternating modulation of the force on the tip, which is used for the determination of the surface potential, see figure 2.

As the potential values are not referenced to a standard potential as in the classical macroscopic Scanning Kelvin Probe (SKP) technique, the Volta-potential maps obtained by means of SKPFM deliver Volta-potential differences on the heterogeneous surface and not absolute potential values. The measurements were performed under ambient conditions in air with a NanoWizard 4 (JPK Instruments, Bruker Nano GmbH) operating with a resolution of 1024×1024 pixels. For the topographic scan, the contact mode was used, whereas for the Kelvin Probe scan the tip was lifted to a predefined height of 40 nm and an AC voltage of 0.8 V was applied to the tip to determine the surface potential following the topography profile. The AFM and SKPFM images were collected at a scan frequency of 0.5-1.0 Hz using a silicon cantilever with a conductive Cr/Pt-coating (Tap300-G tip, Budget Sensors) with a nominal spring constant of 40 N/m. The reported surface potentials values are relative to the potential of the

tip. The software JPK Data Processing Suite 6.1.88 was used for offline analysis of the topographies. To remove tilt and the vertical z-offset between line scans, image flattening was performed with the first order least-square polynomial function.

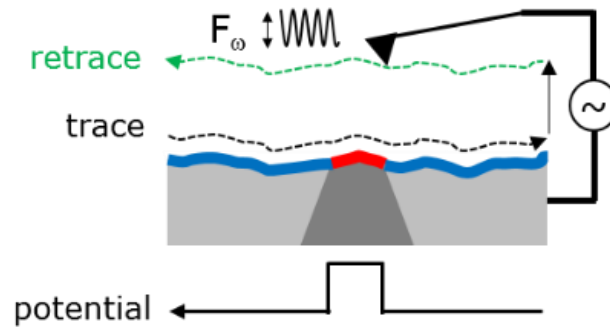


Figure 2. Work principle of SKPFM.

In contrast to the TDS-samples, we only investigated hydrogen charged CoCrNi-samples by AFM. For that purpose, the working electrode was the CoCrNi-sample, counter was graphite rod and reference electrode was Ag/AgCl (for potential measurement during hydrogen charging). The electrolyte had the same composition as used for the TDS-samples. The volume was 10 ml (cm³) and charging current density was 1 mA/cm² applied for 1 and 2 hours.

3 Results and discussion

3.1 Temperature dependent hydrogen diffusion trapping by TDA peak deconvolution

The figures in this subsection show the different hydrogen diffusion and effusion behavior dependent on both the chemical composition and applied Φ . For that purpose, figure 3 shows the obtained different hydrogen effusion spectra for (a) CoCrFeMnNi and (b) CoCrNi for the applied Φ of 0.125 K/s and 0.250 K/s.

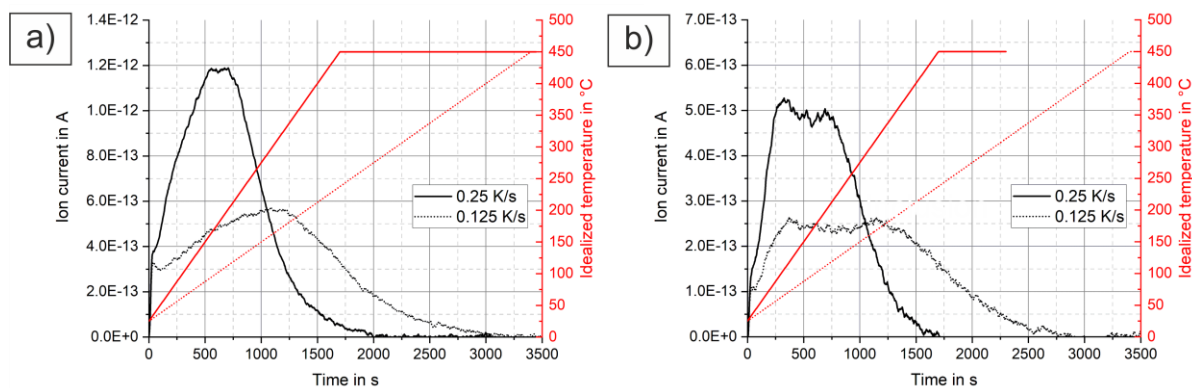


Figure 3. Hydrogen effusion spectra for $\Phi = 0.125$ K/s and 0.250 K/s: (a) CoCrFeMnNi, (b) CoCrNi.

Both materials had quite different hydrogen diffusion behavior. This is expressed by the different maximum ion current and the total effusion time that was necessary to release the hydrogen. In case of the CoCrFeMnNi, a delayed hydrogen diffusion was identified that is expressed by an increased total desorption time (e.g. CoCrFeMnNi with approximately 2000 s compared to 1700 s for CoCrNi at $\Phi = 0.250$ K/s). Both applied heating rates of 0.125 K/s and 0.250 K/s resulted in a shift of the maximum peak value and time of appearance. That corresponds to different peak temperatures and indicates that

e.g. the different atoms within the crystal lattice of the CoCrFeMnNi-HEA and CoCrNi-MEA have significant impact on the hydrogen diffusion, i.e. the predominant trap sites are different. Considering that the integrated spectra correspond to the total desorbed hydrogen, it is obvious that CoCrFeMnNi-HEA (max. ion current $1.19 \cdot 10^{-12}$ A) had a higher absorbed hydrogen concentration compared to the CoCrNi-MEA ($5.17 \cdot 10^{-12}$ A). Detailed hydrogen concentration values are shown in table 3.

The obtained spectra had been subjected to peak deconvolution with an increasing number of peaks. Figure 4 shows the results for the peak deconvolution with two and three peaks for CoCrFeMnNi (parts a, b) and CoCrNi (parts c, d).

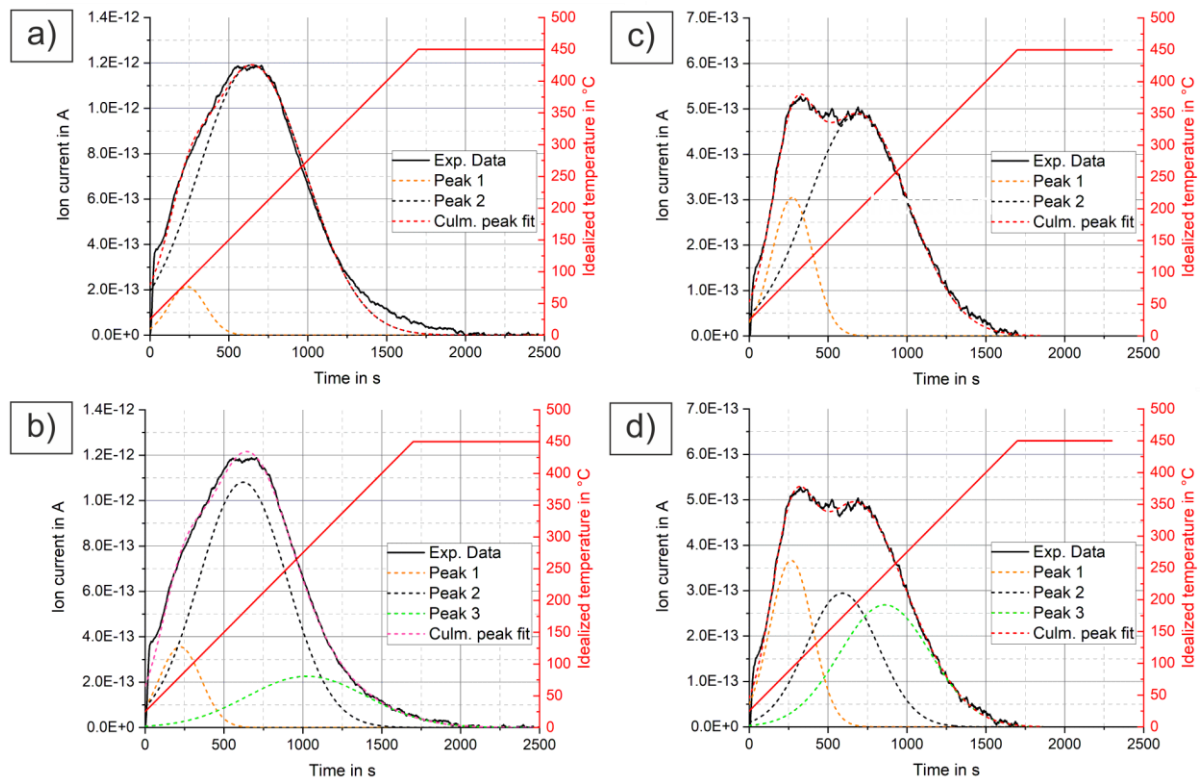


Figure 4. Peak deconvolution at $\Phi = 0.250$ K/s for

CoCrFeMnNi-HEA with 2 peaks (a), 3 peaks (b) and CoCrNi-MEA with 2 peaks (c) and 3 peaks (d)

If the TDS spectra is deconvoluted in two peaks (figure 4 a, c), the first peak always appears in a relatively low temperature range (around 75 °C). A major trap site was identified for both CoCrFeMnNi and CoCrNi at approximately 200 °C. This could already correspond to certain microstructure effects. This interpretation changes if the spectra are deconvoluted into three peaks, see figure 4 (b, d). As a result, the previously mentioned high peak is split into smaller peaks, which results in the appearance of an additional desorption peak (“peak no. 3” in figure 4 (b, d) at higher temperatures.

This indicates that the hydrogen diffusion, i.e. trapping behavior in HEA and MEA materials is generally more complex than already reported [7,15]. For that reason, the number of deconvoluted peaks was increased to four and five as shown in figure 5 (a, b) for CoCrFeMnNi-HEA and (c, d) for CoCrNi-MEA.

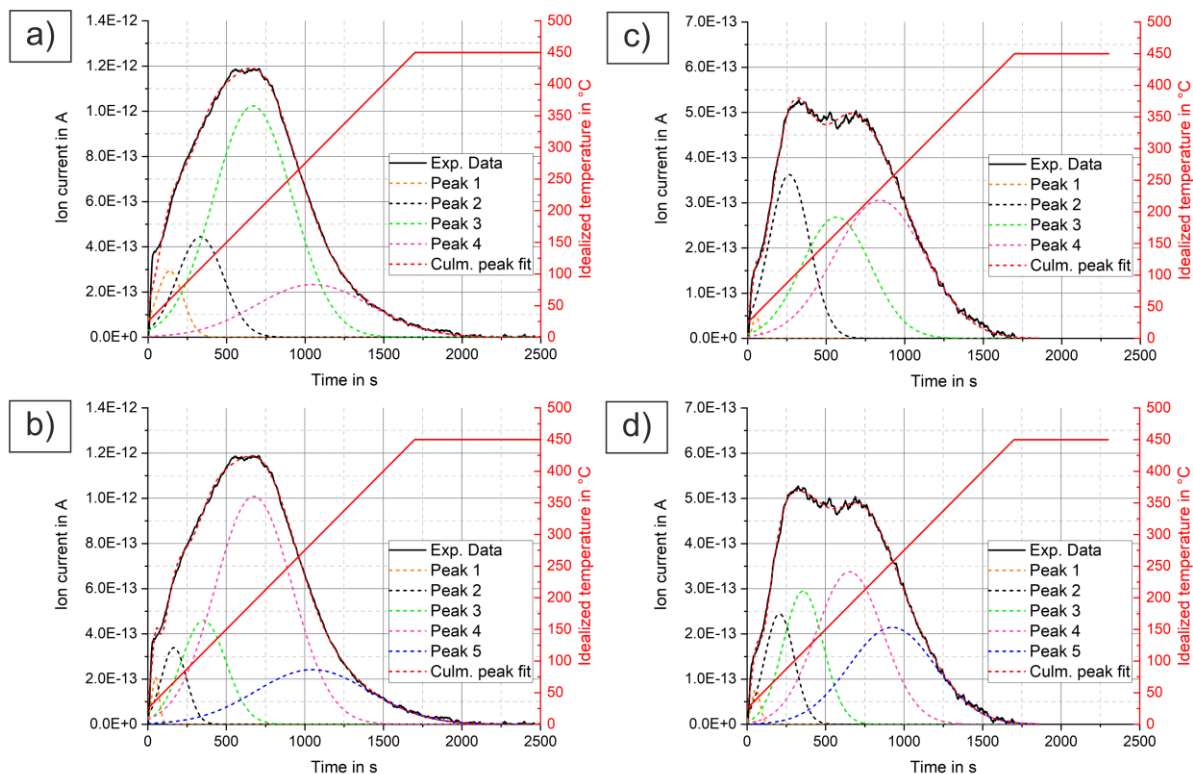


Figure 5. Peak deconvolution at $\Phi = 0.250$ K/s

CoCrFeMnNi-HEA with 4 peaks (a), 5 peaks (b) and CoCrNi-MEA with 4 peaks (c) and 5 peaks (d)

Figure 4 and figure 5 demonstrate the challenges that are anticipated with reliable deconvolution of measured TDA spectra. With the increasing number of deconvoluted peaks to four or five, the quality of the cumulative peak fit increases (R^2 -values see table 2). This is of course a mathematical effect due to the higher number of terms of the fit equation. But there is virtually no difference between the quality of four or five peak fit functions to three peaks, see figure 4 (b, d). The main high temperature peaks do not further change, especially for the CoCrFeMnNi-HEA. But the low temperature peak, $T < 70$ °C, see figure 4 (b, d), can be further expressed as a sum of smaller peaks (see figure 5).

Table 2. Peak deconvolution - model quality.

Amount of peaks	Model quality (R^2)	
	CoCrFeMnNi-HEA	CoCrNi-MEA
2	0.99217	0.99435
3	0.99609	0.99591
4	0.99755	0.99672
5	0.99885	0.99813

This raises the question what microstructure or experimental condition influences the obtained results that justify the number of chosen peaks. As example for experimental condition, it must be considered that the G8 Galileo analyzer is equipped with an infrared furnace. For that reason, the sample surface is heated, and the bulk material is heated by the heat conduction. Hydrogen at the surface near region is activated and desorbs first [30]. This results in apparent experimental-design influenced desorption peaks that have no direct relation to microstructure or chemical composition. If the number of peaks for

the spectra deconvolution is insufficient (i.e. the number of the mathematical terms of the regression model), these apparent peaks are “blurred”. Nonetheless, it is important to identify and to consider those peaks as they have an impact on the further description peaks with real microstructural background in terms of changing the peak temperatures, which could influence the further calculation of activation energies for hydrogen traps [30,36]. In that connection, the five-peak-deconvolution was chosen because it offered the highest model quality (described by R^2 -value, see table 2). For comparison to effusion spectra for $\Phi = 0.250$ K/s, see figure 5 (b, d), figure 6 shows the corresponding five-peak-deconvolution of for $\Phi = 0.125$ K/s for (a) CoCrFeMnNi and (b) CoCrNi.

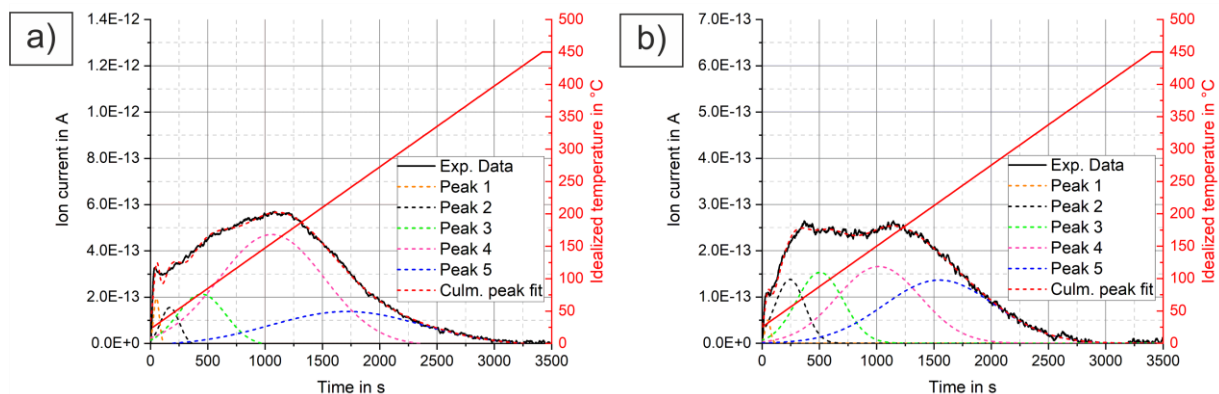


Figure 6. Peak deconvolution with five peaks at 0.125 K/s:
(a) CoCrFeMnNi / $R^2 = 0.99634$, (b) CoCrNi / $R^2 = 0.99166$.

Especially, at lower heating rate of 0.125 K/s a reliable peak deconvolution is necessary. As mentioned, the peaks at low temperatures (peak 1 and 2 for CoCrFeMnNi below 50 °C and for CoCrNi below 60 °C) could be unique experimental effects of the CGHE. Nonetheless, both materials showed a significant hydrogen effusion for nearly 3,500 s (CoCrFeMnNi) and 3,000 s (CoCrNi) despite the continuous increasing temperature up to 450 °C. Considering the small sample thickness of 2.0 mm (see figure 1), the hydrogen diffusion in both materials is very slow. This was already reported for CoCrFeMnNi-HEA [7,15], but is new for CoCrNi-MEA material, especially the significant hydrogen release at elevated temperatures above 100 °C.

3.2 Corresponding peak temperatures and hydrogen concentration

This subsection presents the data for the 5-peak-deconvolution for both materials and applied heating rates Φ of 0.125 K/s and 0.250 K/s with respect to the hydrogen concentration of each peak (HD_{PX} , where “PX” is the peak no. 1 to 5) and the total hydrogen concentration (HD_{tot}). The corresponding hydrogen release temperature encompasses the peak temperature (T_P), i.e. the temperature of the maximum effusion rate for the respective peak. The data are presented and summarized in table 3. The corresponding peak temperatures are presented (for presentation purposes) as integer values. The reason is the negligible difference for 1 °C temperature increment if the underlying Φ -dependent time interval is considered (0.125 K/s corresponds to 8 s increment time vs. 3,400 s total heating time and for 0.250 K/s corresponds to 4 s vs. 1,700 s).

Table 3. Peak dependent HD_{PX} and total hydrogen concentration HD_{tot} with corresponding release/desorption temperatures.

	Φ	Value	Unit	Peak number HD_{PX}					Total
				1	2	3	4	5	
CoCrFeMnNi-HEA	0.125 K/s	HD	[ppm]	2.3	4.8	13.3	41.1	52.5	114.0
				± 0.9	± 1.0	± 0.5	± 15.1	± 25.1	± 11.3
		HD	[%]	2	4	12	36	46	100
			± 1	± 1	± 0.5	± 13	± 22	± 10	
	T_p	[°C]	31	43	70	128	200	-	
			± 1	± 3	± 11	± 27	± 28	-	
0.250 K/s	HD	[ppm]	1.1	10.8	25.7	70.5	20.1	128.4	
			± 0.2	± 3.3	± 7.3	± 0.9	± 4.4	± 7.0	
	HD	[%]	1	8	20	55	16	100	
		± 1	± 1	± 1	± 13	± 22	± 5		
T_p	[°C]	38	73	121	197	286	-		
		± 1	± 6	± 8	± 3	± 1	-		
CoCrNi-MEA	0.125 K/s	HD	[ppm]	0.4	4.4	8.7	16.6	14.9	45.0
				± 0.2	± 0.2	± 1.3	± 2.2	± 1.1	± 2.8
		HD	[%]	1	10	19	37	33	100
			± 0.5	± 0.5	± 3	± 5	± 2	± 6	
	T_p	[°C]	32	56	90	154	221	-	
			± 1	± 1	± 2	± 2	± 2	-	
0.250 K/s	HD	[ppm]	0.7	4.8	10.1	22.5	16.0	54.1	
			± 0.2	± 0.6	± 1.4	± 5.8	± 2.4	± 9.2	
	HD	[%]	1	9	19	42.5	29.5	100	
		± 1	± 1	± 3	± 11	± 4	± 17		
T_p	[°C]	39	74	110	184	257	-		
		± 0	± 3	± 4	± 4	± 1	-		

The data in table 3 indicate that a complex hydrogen trapping behavior must be anticipated in both HEA and MEA (whereas the deviation was quite high for the lower heating rate of $\Phi = 0.125$ K/s). The CoCrFeMnNi-HEA trapped a significantly higher hydrogen concentration (mean value of 114.0 ppm for $\Phi = 0.125$ K/s; 128.4 ppm for $\Phi = 0.250$ K/s) compared to CoCrNi-MEA (mean value 45.0 ppm for $\Phi = 0.125$ K/s; 54.1 ppm for $\Phi = 0.250$ K/s), which corresponds to a factor of approximately 2.5. The measured absorbed hydrogen concentration of CoCrNi-MEA corresponds to fcc-material like austenitic stainless steels [37] with approximately 40 ppm. The CoCrFeMnNi showed absorbed hydrogen concentration that is in the same range, but is higher compared to the reported 70 ppm for CoCrFeMnNi [7,15]. The increased number of equiatomic elements of CoCrFeMnNi-HEA must offer an increased number of hydrogen traps compared to the CoCrNi-MEA. This is important if those materials are exposed to hydrogen. Nonetheless, the mechanical behavior suggests superior resistance against hydrogen assisted cracking (or hydrogen embrittlement) of CoCrFeMnNi-HEA [7,9] and CoCrNi-MEA [10].

Peak no. 1 and no. 2 appeared for both heating rates and materials in the lower temperature regions, considering figure 5 (b, d) for $\Phi = 0.125$ K/s and figure 6 (a, b) Φ of 0.250 K/s. Especially peak no. 1 always occurred close to the initial start temperature (30-32 °C). But the second peak appeared between 46 to 74 °C. In addition, they correspond to approximately 1 to 2 % for peak no. 1 and 4 to 10 % for peak no. 2 of the totally absorbed hydrogen concentration. This results in apparent desorption peaks that have no direct relation to microstructure or chemical composition. But if these peaks are not separated,

they could “blur” real microstructure dependent peaks during hydrogen measurement. The low temperatures are perhaps the result of two effects of the experimental procedure respectively the data acquisition. Effect (1): The specimen has a localized small hydrogen enriched subsurface region due to the charging, i.e. a concentration gradient. A worst-case scenario for that is when the so-called blistering occurs [38,39]. In addition, the adsorbed hydrogen could be trapped (by an increased number of dislocations) because of the mechanical surface preparation [40,41] (in our case the grinding and polishing process). In addition, a pronounced texture could have an effect on the grain orientation. In addition, it is difficult to measure this thin subsurface hydrogen enriched “layer” thickness as CGHE does not allow localized hydrogen measurement. Effect (2): The use of infrared radiation is assumed to activate at first the hydrogen in this enriched region close to the specimen surface. The reason is that the heat was coupled into the specimen via the surface. Subsequently, the bulk was heated by thermal conductivity resulting in a “delay” of the higher temperature. This supports the assumption that the sample surface near hydrogen is activated very fast and must desorb first [30].

Peaks no. 3 to 5 represent microstructure, i.e. chemical composition, influenced effusion peaks. They encompass nearly 90 % of the total absorbed hydrogen. This means that in case of the CoCrFeMnNi-HEA more than 100 ppm hydrogen can be trapped at elevated temperatures. If the different heating rates are considered, peak no. 4 and 5 encompass 71 - 83 % of the absorbed hydrogen concentration with high hydrogen desorption peak temperatures within the range from 157 to 282 °C. A similar behavior was found for the CoCrNi-MEA from 154 to 256 °C. That indicates that the general diffusion behavior of both CoCrFeMnNi and CoCrNi represent typical fcc-lattice hydrogen diffusion behavior like austenitic stainless steels. But in case of the CoCrFeMnNi-HEA, the absorbed hydrogen concentration is much higher. It is believed that due to a similar average grain diameter, the grain boundaries volume as a predominant difference between both CoCrFeMnNi-HEA and CoCrNi-MEA can be excluded. Nonetheless, grain boundaries in fcc-metals can show increased numbers of dislocations. If the number of dislocations increases, the number of hydrogen traps increases and, for that reason, the absorbed and trapped hydrogen concentration [42]. This could be an explanation for the significantly increased trapped hydrogen concentration but demands e.g. further investigations on dislocation density. The lattice distortion of HEA and MEA as a predominant difference between both alloy types can also be excluded. It was shown that CoCrFeMnNi-HEA and CoCrNi-MEA had similar distorted lattices and, for that reason, no significant differences between the fcc-lattice strains [43].

It currently remains open, which predominant trap is the most important difference between hydrogen trapping in CoCrFeMnNi-HEA and CoCrNi-MEA, which is described by the significantly different hydrogen trapping (factor 2.5). Additional experiments with Time-of-Flight secondary ion mass spectroscopy will reveal predominant hydrogen trap sites in the material. Currently, the correlation of traps, i.e. distinct microstructure effects, in terms of calculation of activation energy E_A is difficult as we only investigated two heating rates (possible shift of Arrhenius-regression functions). For that reason, a heating rate $\Phi = 0.625$ K/s will be applied to determine a third set of the peak temperatures of peak no. 1 to no. 5. This enables determination of activation energies for the corresponding hydrogen traps via an Arrhenius-relationship between the heating rate Φ and the peak temperature T_P [30,31].

3.3 Local Volta potential maps by SKPFM

SKPFM was used to determine the surface topography and Volta potential differences at the same region of interest. Figure 7 shows the results of the CoCrFeMnNi-HEA. For that purpose, parts (a) and (b) included the topographic scans and parts (c) and (d) the corresponding local Volta potential maps. The upper row presents a scan area of 100 x 100 μm and the lower row 25 x 25 μm . Figure 8 shows the corresponding CoCrNi-MEA results (for 100 x 100 μm scan area). For comparison, the corresponding topographic images were presented together with the work function map.

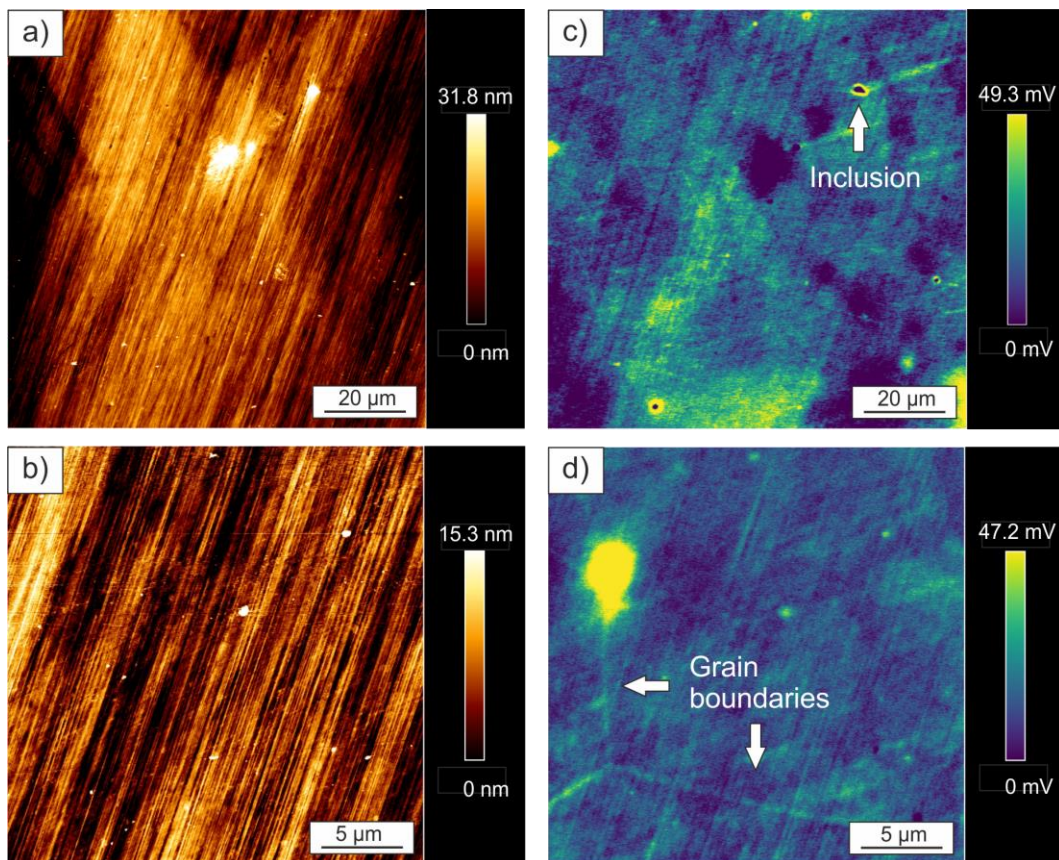


Figure 7. Uncharged CoCrFeMnNi-HEA: (a, b) topographic scan (c, d) local Volta potential.

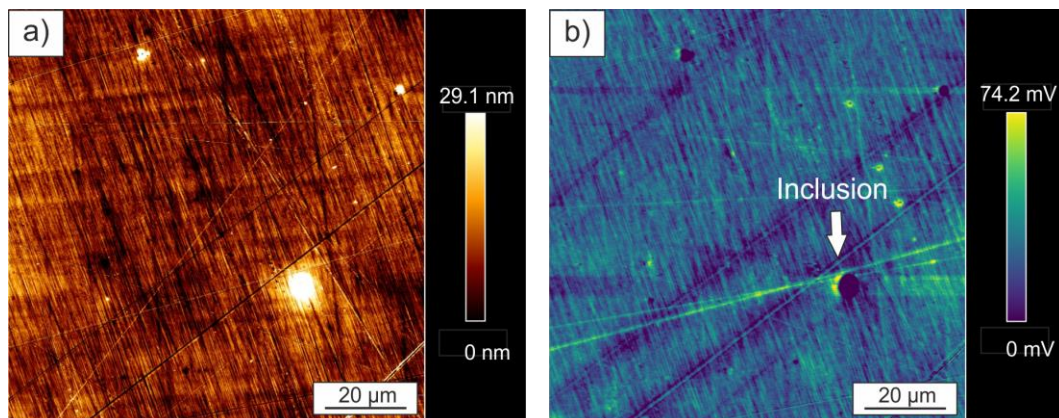


Figure 8. Uncharged CoCrNi-MEA: (a) topographic scan and (b) local Volta potential.

In all images the direction of the polishing is discernible, however the polishing lines are more pronounced in the topographic scans than in the work function / SKPFM images, as the latter tracks the topography scan during the acquisition of the potential profiles. High and low work function regions are clearly visible in the topography scans and indicate that different phases are present in the surface of both materials. This was already reported for CoCrFeMnNi-HEA [44,45]. To identify what phases these, work function areas correspond to a combination with other imaging techniques such as EBSD will be required. Another feature in case of the CoCrFeMnNi-HEA (figure 7) are grain boundaries, which are indicated by lines of higher potential (figure 7 d) that are not visible in the topographic image, see

figure 7 (b). The CoCrNi SKPFM image does not show grain boundaries as the measured lines, as indicated in figure 8 (b), are of distinguishable potential but not clearly discernible from the surrounding matrix. Nevertheless, both SKPFM images of CoCrFeMnNi-HEA and CoCrNi-MEA enable the visualization of inclusions or other forms of impurities in the material that had not been observed in the topographic image (parts a). In the recorded SKPFM images this can be deduced by the spots of low potential surrounded by a rim of high potential. It is assumed that these inclusions / impurities are oxides, which are already in the material (during casting and processing) or form during the preparation of the samples for SKPFM. Considering the SKPFM work function, thick and pure oxides are a reasonable explanation as they have very low electrical conductivity, i.e. high electrical resistance and virtually suppress the measuring of any potential. This supports the result of areas with low Volta potential that are surrounded by high potential rims. These inclusions could be Al-rich (as a result of the processing route using Al-rich crucibles) [28] or further Cr- und Mn-oxides [29,46]. It remains open if inclusions generally are a considerable factor for application relevant properties like corrosion resistance (formation of galvanic elements vs. pitting). In accordance to [47], Al leads to microstructural changes, which in turn, were manifested to result in selective dissolution of Al and Al-rich phases. To identify the chemical composition and what these inclusions correspond to, a combination with other imaging techniques (like ToF-SIMS) will be required. To determine a possible hydrogen charging effect on the local Volta potential, a CoCrNi-sample was hydrogen-charged for 1 hour at 1 mA/cm² and investigated and again after 2 hours of charging time. The results are shown in figure 9. Parts (a) and (b) include the topographic scans and parts (c) and (d) the local Volta potential maps (scan area of 100 x 100 μm).

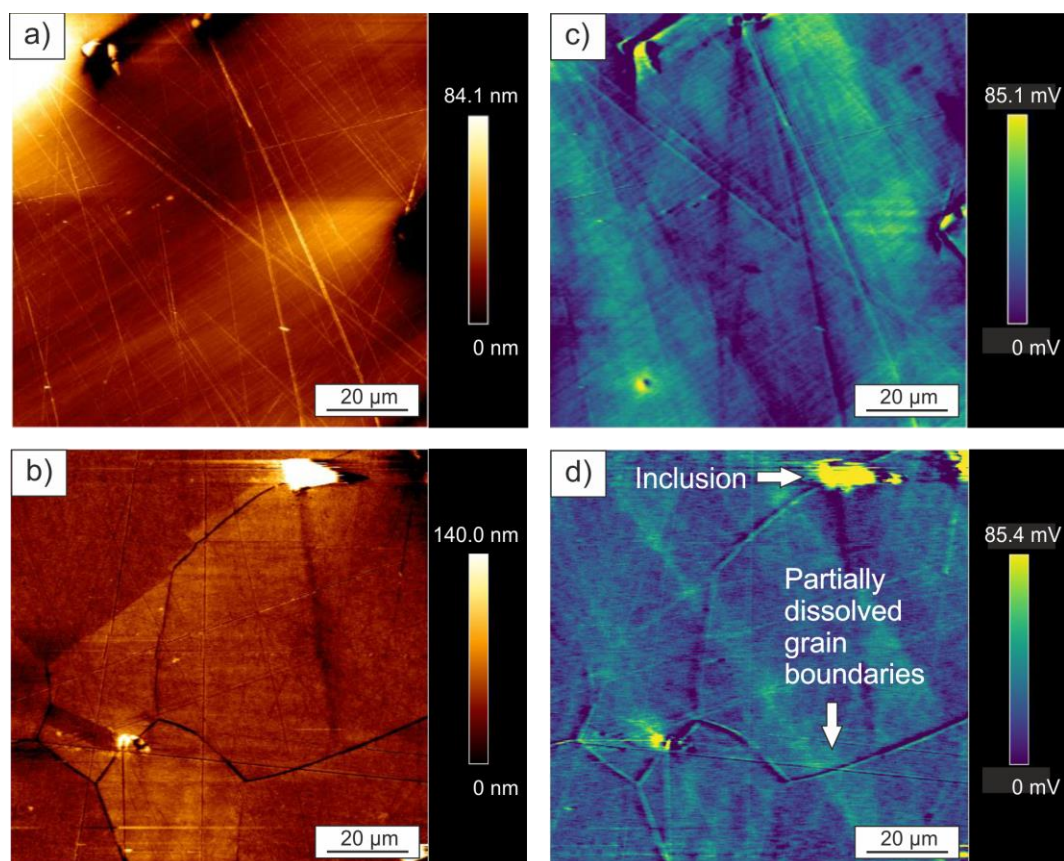


Figure 9. Hydrogen charged CoCrNi-MEA with 1 A/cm² for 1 h: (a) topographic scan, (c) local Volta potential; for 2 h: (b) topographic scan and (d) local Volta potential.

If compared to the reference condition (see figure 8), the hydrogen charging did not result in remarkable changes in the local potential (approximately 85 mV in charged condition to 78 mV in hydrogen

free condition, whereas these are maximum values determined at inclusions). The homogenous potential distribution in hydrogen charged condition (parts c and d) is assumed to be a result of the limited hydrogen charging time of 1 and 2 hours. This time is rather short if it is considered that the examined MEA material has an austenitic crystal lattice and, hence, a very low hydrogen diffusion coefficient. The result is that hydrogen needs certain time to accumulate at crystal defects like inclusions or penetrate the bulk material. Hence, only a sub-surface near region could be perhaps enriched with hydrogen. Nonetheless, a significant effect of hydrogen on local potential is assumed in accordance to [48]. The hydrogen charging resulted in a surface degradation as indicated by an intergranular corrosion-like preferred dissolution of grain boundary areas in case of 2 h hydrogen charging (see figure 9 b). Currently, it remains open if the obviously dissolved areas are result of the charging parameters (as TDS-samples had been subjected too much longer exposition time at higher current density). It could be also a result of the local corrosion resistance of the MEA material. Although CoCrNi-MEA should have a homogenous distribution of the alloy elements [10], the ion concentration in the residual electrolyte was Cr-enriched and suggests that this element was preferably dissolved. But this experimental finding is still an assumption. For that reason, the combination of hydrogen charged HEA and MEA samples and corresponding SKPFM analysis must be investigated more detailed.

4 Summary and conclusions

In this study, we investigated the CoCrFeMnNi-HEA and CoCrNi-MEA. Cathodic hydrogen charging was applied and measured by high-resolution TDS with MS. For identification of temperature dependent diffusion, two different heating rates $\Phi = 0.125$ and $\Phi = 0.250$ K/s had been applied. Local surface topography and Volta potential scans were by SKPFM and compared for the hydrogen free condition and for CoCrNi in hydrogen charged condition. The following conclusions can be drawn from this study:

- A minimum number of peaks is needed for reasonable deconvolution of TDS hydrogen desorption spectra and five peaks had been suitable in our results. It was ascertained that at least peak no. 1 and (partially) no. 2 is perhaps a result of the applied CGHE technique (in terms of the used furnace type). This is supported by the summarized amount of max. 10 % of the total absorbed hydrogen concentration.
- High-temperature desorption peaks occurred in both materials, which indicates that high energies are necessary for the release of hydrogen from the respective trap. If the different heating rates are considered, peak no. 4 and 5 encompass 71 to 83 % of the absorbed hydrogen concentrations. This indicates two important effects: (1) delayed hydrogen diffusion and (2) a considerable amount of trapped hydrogen also at high temperatures that must be anticipated for hydrogen assisted cracking.
- The CoCrFeMnNi-HEA showed trapped hydrogen within a temperature range from 157 to 282 °C and CoCrNi-MEA from 154 to 256 °C if the respective peak temperatures are considered. Both HEA and MEA have comparable hydrogen diffusion characteristic that are additionally like other fcc-materials for example high-alloyed austenitic stainless steels. The absorbed hydrogen concentration was higher than 100 ppm for both heating rates in case of the CoCrFeMnNi-HEA, which was significantly higher than the approximately determined 40 ppm in case of the CoCrNi-MEA. It currently remains open, which predominant trap is the difference between hydrogen trapping in CoCrFeMnNi HEA and CoCrNi MEA. For calculation of activation energies for hydrogen trapping and release, further experiments with another heating rate are necessary.
- SKPFM investigations showed that both materials CoCrFeMnNi and CoCrNi contained inclusions/impurities that could be identified in the topography and Volta potential scans. The inclusions are assumed to be oxides, but further investigation is necessary to draw reliable conclusions. Their impact on possible application relevant properties such as corrosion resistance (depending on the electrolyte accompanied with hydrogen evolution and further hydrogen assisted cracking phenomena like stress corrosion cracking) is topic of ongoing research.

- Hydrogen charging of CoCrNi-MEA caused no obvious differences in the local Volta potential in case of the applied charging parameters. This is perhaps an experimental effect and suggests that hydrogen charging (as a combination of the material and the applied charging parameters) must be conducted carefully.

Acknowledgements

The authors want to thank Prof. Guillaume Laplanche (Ruhr-University, Bochum, Germany) for providing the experimental materials and further processing information. Prof. Christiane Stephan-Scherb and Dr. Wencke Schulz are thanked for materials characterization as well as Mr. Jirka Biermann for the machining of the samples (all with BAM Berlin, Germany).

References

- [1] Yeh J W, Chen S K, Lin S J, Gan J Y, Chin T S, Shun T T, Tsau C H and Chang S Y 2004 *Adv. Eng. Mater.* **6** (5) 299–303
- [2] Gali A and George E P 2013 *Intermetallics* **39** 74–78
- [3] Gludovatz B, Hohenwarther A, Catoor D, Chang E H, George E P and Ritchie R O 2014 *Science* **345** 1153–58
- [4] Wu Z, Bei H, Pharr G M and George E P 2014 *Acta Mater.* **81** 428–41
- [5] Schneider M, George E P, Manescau T J, Zalezak T, Hunfeld J, Dlouhy A, Eggeler G and Laplanche G 2020 *Int. J. of Plast.* **124** 155–69
- [6] Laplanche G, Schneider M, Scholz F, Frenzel J, Eggeler G and Schreuer J 2020 *Scripta Mater.* **177** 44–48
- [7] Zhao Y, Lee D H, Seok M Y, Lee J A and Phaniraj M P 2017 *Scripta Mater.* **133** 54–58
- [8] Pu Z, Chen Y and Dai L H 2018 *Mater. Sci. Eng. A* **736** 156–66
- [9] Luo H, Li Z and Raabe D 2017 *Sci. Rep.* **7**, Article number 9892
- [10] Soundararajan C K, Luo H, Raabe D and Li Z 2020 *Corros. Sci.* **167** 108510
- [11] Pressouyre G M 1979 *Metal. Trans. A* **10** 1571–1573
- [12] Grabke H J and Riecke E 2000 *Mater. Tehnol.* **34** 331–42
- [13] Kannengiesser T and Boellinghaus Th 2013 *Weld. World.* **57** 3-37
- [14] Rhode M, *Hydrogen diffusion and effect on degradation in welded microstructures of creep-resistant low-alloyed steels* (Berlin: BAM-Dissertationsreihe 148)
- [15] Lee J, Park C, Park H and Kang N 2020 *Int. J. Hydrogen Energ.* **45** 10227–32
- [16] Boellinghaus Th, Hoffmeister H and Middel C 1996 *Weld. World.* **37** 16–23
- [17] Chen Y, Santos D M F and Sequeira C A C 2006 *Defect and Diffusion Forum* **258-260** 322–26
- [18] Chen Y Y, Duval T, Hung U D, Yeh J W and Shih H C 2005 *Corros. Sci.* **47** 2257–79
- [19] Lee C P, Chang C C, Chen Y Y, Yeh J W and Shih H C 2008 *Corros. Sci.* **50** 2053–60
- [20] Hernandez-Rodriguez M A L, Laverde-Catano D A, Lozano D, Martinez-Cazeres G and Bedolla-Gil Y 2019 *Metals* **9** 307
- [21] Tang Z, Gao M C, Diao H and Yang T 2013 *JOM* **65** 1848–58
- [22] Otto F, Yang Y, Bei H and George E P 2013 *Acta Mater.* **61** 2628–38
- [23] Liu W H, Wu Y, He J Y, Nieh T G and Lu Z P 2013 *Scripta Mater.* **68** 526–29
- [24] Rodriguez A, Tylczak J H and Ziomek-Moroz M 2017 *ECS Transactions* **77** 741–52
- [25] Luo H, Li Z, Mingers A M and Raabe D 2018 *Corros. Sci.* **134** 131–39
- [26] N N 2003 *ASM Handbook, Vol. 13 - Corrosion* ed S D Cramer S D and Covino B S (Materials Park, Ohio: ASM International)
- [27] N N 2011 *Uhlig's Corrosion Handbook* (3rd edition) ed R W Revie (New York: Wiley & Sons)
- [28] Laplanche G, Berglund S, Reinhart C, Kostka A, Fox F and George E P 2018 *Acta Mater.* **161** 338–51

- [29] Richter T, Schroepfer D, Rhode M and Boerner A 2020 Influence of modern machining processes on the surface integrity of high-entropy alloys *IOP Conference Series, Materials Science and Engineering* Symposium on Materials Science and Joining Technology, Magdeburg, Germany (in review)
- [30] Rhode M, Mente T, Steppan E, Steger J and Kannengiesser T 2018 *Weld. World.* **62** 277–87
- [31] Enomoto M, Hirakami D and Tarui T 2011 *Metall. Mater. Trans. A* **43A** 572–81
- [32] Salmi S, Rhode M, Jüttner S and Zinke M 2015 *Weld. World.* **59** 137–44
- [33] Rhode M, Schaupp T, Muenster C, Mente T, Kannengiesser T and Boellinghaus T, *Weld. World.* **63** 511–26
- [34] Yasakau K A, Giner I, Vree C, Ozcan O, Grothe R, Oliveira A, Grundmeier G, Ferreira M G S and Zheludkevich M L 2016 *Appl. Surf. Sci.* **389** 144–56
- [35] Rohwerder M, Hornung E and Stratmann M 2003 *Electrochim. Acta* **48** 1235–43
- [36] Steppan E, Mantzke P, Steffens B, Rhode M and Kannengiesser T 2017 *Weld. World.* **61** 637–48
- [37] Yagodzinsky Y, Todoshchenko, Papula S and Hänninnen H 2010 *Steel Res. Int.* **82** 1–6
- [38] Griesche A, Dabah E, Kannengiesser T, Kardjilov N, Hilger A and Manke I 2014 *Acta Mater.* **78** 14–22
- [39] Perez-Escobar D, Minambres C, Duprez L, Verbeken K and Verhaege M 2011 *Corros. Sci.* **53** 3166–76
- [40] Frappart S, Oudriss A, Feaugas X, Creus J, Bouhattate J, Thebault F, Delattre L and Marchebois H 2011 *Scripta Mater.* **65** 859–862
- [41] Legrand E, Oudriss A, Frappart S, Creus J, Feaugas X and Bouhattate J 2014 *Int. J. Hydrogen Energ.* **39** 1145–55
- [42] Oudriss A, Creus J, Bouhattate J, Savall C, Peraudeau B and Feaugas X 2012 *Scripta Mater.* **66** 37–40
- [43] Owen L R, Pickering E J, Playford H Y, Stone H J, Tucker M G and Jones N G 2017 *Acta Mater.* **122** 11–18
- [44] Hasannaemi, V, Ayyagari A V, Muskeri S, Salloom R and Mukherjee S 2019 *npj. Mater. Degrad.* **3** 16
- [45] Shi Y, Collins L, Feng R, Zhang C, Balke N, Liaw P K and Yang B 2018 *Corros. Sci.* **133** 120–31
- [46] Schulz W, Laplanche G, Schneider M, Karafiludis S and Stephan-Scherb C 2020 Insights into the high temperature oxidation behavior of the equiatomic CrMnFeCoNi and CrCoNi high- and medium-entropy alloys *Oxid. Met.* (in review)
- [47] Yao Q, Thomas S, Gibson M A, Fraser H L, and Birbilis N 2017 *npj. Mater. Degrad.* **1** 15
- [48] Nazarov A, Vucko F and Thierry D 2020 *Corros. Mater. Degrad.* **1** 9–20